Available online at www.sciencedirect.com
SCIENCE DIRECT®
PERGAMON
International Journal of Multiphase Flow 29 (2003) 1183–1192
International Journal of Multiphase Flow
www.elsevier.com/locate/ijmulflow

Brief communication

Particles resuspension in waves using visualization and PIV measurements — coherence and intermittency

U. Shavit *, S. Moltchanov, Y. Agnon

Department of Civil and Environmental Engineering, Technion, Israel Institute of Technology, 32000 Haifa, Israel

Received 1 January 2003; received in revised form 2 April 2003

1. Introduction

Many contemporary resuspension models assume diffusive sediment entrainment processes and apply empirical pick-up functions to define the bottom boundary condition (e.g. Nielsen, 1992). These pick-up functions provide an integral description while ignoring the spatial and temporal distributions of the resuspension phenomena. However, the importance of intra-wave processes has been noted in several studies, showing that resuspension occurs in particular phases of the wave cycle (e.g. Black and Vincent, 2001) and at particular spatial locations within the wavelength. Particle image velocimetry (PIV) with triggering capability has the potential to reveal new insight into the subject of suspended particles transport with relation to spatio-temporal correlations of resuspension events and the flow field.

Many studies show that resuspension is likely to occur at times and regions of high shear. Others have shown that resuspension occurs when the velocity field changes its sign (Black and Vincent, 2001). The existence of bars and ripples and their remarkable impact on vortex shedding led to a large number of studies that investigated resuspension over topographical features (Blondeaux, 2001). The effect of such features dominates the bottom velocity field and the mechanism of particles entrainment. However, as resuspension is also observed on a flat bed (Black and Vincent, 2001), its fundamental physical mechanisms should be studied. Numerous investigations have addressed mechanisms, which take place inside the bottom boundary layer and are important for understanding and describing the transport via bed-load and sheet flow. For particles that have a larger residence time in the water column, and for processes that occur in the core of the flow field, it is important to study the resuspension beyond the boundary layer. The present study focuses on the entrainment of suspended particles upwards from the boundary layer, into the fluid core.

* Corresponding author. Tel.: +972-4-829-3568; fax: +972-4-822-1529.
E-mail address: aguri@tx.technion.ac.il (U. Shavit).

0301-9322/03/$ - see front matter
doi:10.1016/S0301-9322(03)00066-1

In this preliminary study we have applied PIV for both visualization and velocity measurements. Fine particles were introduced into a small-scale wave flume. The spatio-temporal variations of resuspension events, the location of sediment ejections and the spatial transport patterns were investigated.

2. Experimental methods

A glass flume (200 cm long, 10 cm high and 5 cm wide) was filled with 5 cm depth of distilled water and used to generate a standing wave flow regime (Fig. 1). A pneumatic system and a programmable controller (Bakara, Geva, Israel) controlled a piston-type wave generator. Its horizontal displacement is nearly harmonic: $\xi(t) \approx A\cos(2\pi t/T)$ where A is 1.75 cm and T is 400 ms.

Two types of particles were used; seeding (tracer) particles and sediment particles. Both were separated from a batch of hollow glass spheres (Potters, USA). The volumetric mean diameter of the two groups of particles was measured by laser diffraction (Coulter LS230, Beckman, USA) and found to be $d = 11.7$ μm in both groups. The density of the sediment and tracer particles was $\rho_{sed} = 2.12$ gr/cm^3 and $\rho_{tr} = 1$ gr/cm^3 respectively. These density differences are due to size variations of the internal air bubble inside the hollow glass spheres. The Stokes number of the tracer particles was $\sim 10^{-3}$ ($St = (\rho_{tr} g d^2)/(18\mu U)$, where g is gravity, μ is the fluid viscosity, and U is mean velocity).

The PIV system is composed of a 160 mJ per pulse Nd:YAG double laser system (Twins, Quantel, France) and a cross correlation eight bit 1K × 1K CCD camera (Kodak, MEGAPLUS ES 1.0, USA). The Laser beams were directed as shown in Fig. 1 to align the flume with the wave generator and to illuminate the flow field. A uniform interrogation area of 32 × 32 pixels with 50%

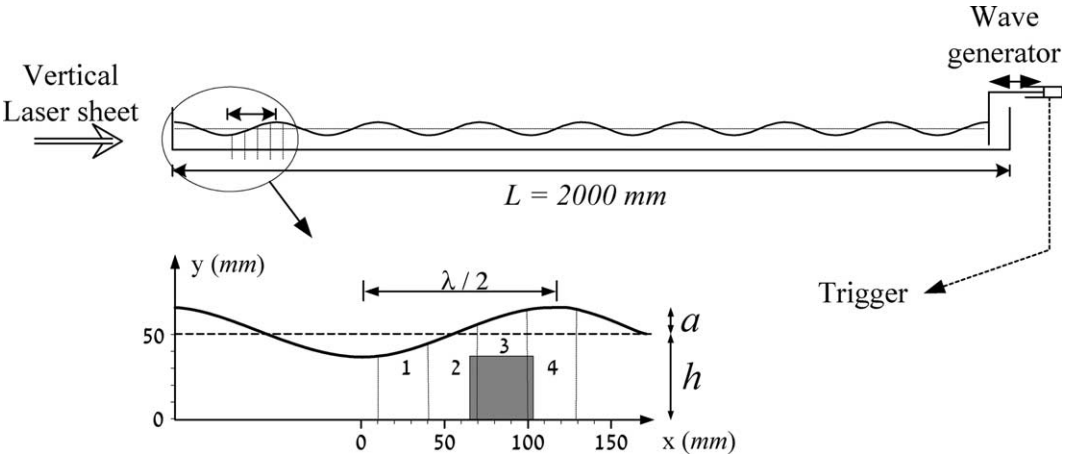

Fig. 1. The experimental setup. The paper presents results from region #3 only. The origin of the x-axis is at an anti-node located to the left of region #3. The first node is at $x \sim 56$ mm and the second anti-node is at $x \sim 112$ mm. λ is ~225 mm, $h = 5$ cm, $a = 1.24$ cm.

overlay results in about 3780 velocity vectors. The micron-to-pixel ratio was 39.7 μm/pixel, resulting in a measurement window size of 38 mm × 38 mm. As the time between pulses was adjusted to maintain a mean translation of 3–5 pixels, the estimated PIV error is 2–4%. The vector validation rate was very high. The maximum rejection rate was between 3.9% (tracer particles) and 5% (sediment particles), applying first a signal-to-noise filter (that identified more than 80% of the outliers) followed by a local median filter. Further rejection due to other filters was nearly zero.

Following the distribution of a thin layer of particles, the wave generator was turned on, operating for at least three hours before measurements took place. At these equilibrium conditions the reflection coefficient of the partial standing wave was ~0.9 with a wave amplitude of 1.24 cm and a wavelength of $\lambda = 225$ mm. The wave Reynolds number, $Re = A_b^2\omega/\nu$ was 898 where A_b is the semi excursion length of the orbital motion, ω is the wave angular frequency and ν is the molecular viscosity (Dohmen-Janssen, 1999). The particle Reynolds number, $Re_p = A_b\omega d/\nu$ is 1.54. Visualization and PIV velocity measurements were obtained using triggering and phase delay at a frequency equal to the wave generator frequency. The experiment was repeated 16 times, 200 periods each. The instantaneous velocity field was sampled once every period, at a (different) constant phase for each of the 16 runs. This instantaneous velocity, $V = ui + vj$, was decomposed into two components; the periodic velocity component, $\overline{V}$, and the turbulent velocity, V'. The periodic velocity, $\overline{V}$, was obtained by applying an ensemble average based on the 200 realizations,

$$\overline{V}^i = \frac{1}{200}\sum_{j=1}^{200} V^{ij} \tag{1}$$

i indicates the phase and j the realization. This procedure provides 16 vector fields within the wave period ($\Delta t = 25$ ms). The time-averaged velocity, V_s, was obtained by applying an ensemble average utilizing all the realizations as follows:

$$V_s = \frac{1}{200 \times 16}\sum_{i=1}^{16}\sum_{j=1}^{200} V^{ij} = \frac{1}{16}\sum_{i=1}^{16}\overline{V}^i. \tag{2}$$

These velocity fields were measured in regions #1–#4 (Fig. 1), however, the results shown throughout the paper are taken from region #3. The measurements were performed twice, applying separately tracer particles and sediment particles.

3. Results and discussion

3.1. Visualization

Our observations reveal that resuspension events occur intermittently and last for a few periods. These observations are demonstrated in Fig. 2, which shows a section within region #3. Sediment particles are accumulated near the flume floor under the node, move horizontally in the boundary layer until they reach the location from which resuspension events take place. Particles

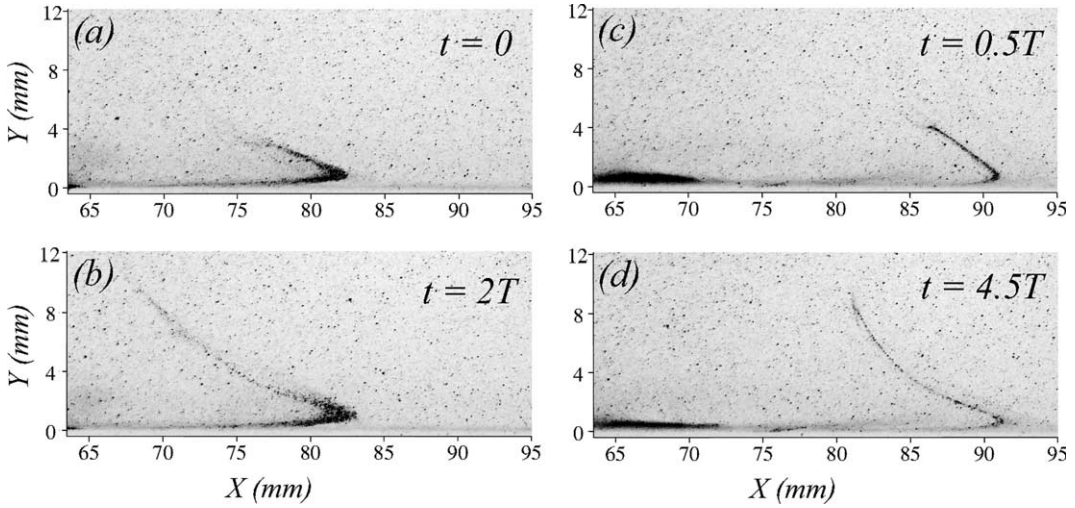

Fig. 2. Images of two series of resuspension events (a and b at $t = 0$ and $t = 2T$, c and d at $t = 0.5T$ and $t = 4.5T$). Note, the resuspension location and streaks evolution.

then form intermittently coherent thin streaks, which take the particles towards the upper left corner of the image. Most of these particles continue to move upwards and join a large clockwise re-circulation. Others descend under the node and form a rippled pattern on the floor. A very similar but not perfectly symmetric image of bed-form, boundary layer dynamics and sediment transport was observed on the other side of the nodal and anti-nodal regions.

The images in Fig. 2a and b were captured at the beginning of the wave period (zero phase) when the velocity is zero and the lower anti-node is on the right (at $x \sim 112$ mm). The images (shown in negative) represent a sequence of two consecutive wave periods and indicate that the particles streak moves vertically at a speed of roughly 3 mm/period = 0.0075 m/s. The figure shows that at zero phase of the particular observation, resuspension location was around $x = 82$ mm (0.36λ). As expected, the location of resuspension oscillates. Fig. 2c and d show that the instantaneous resuspension location was around $x = 91$ mm (0.4λ) at $t = T/2$. We will show that the resuspension location correlates with the location of high shear. Fig. 2c and d provide an observation of the bed-load motion, represented by the dense, dark, regions on the floor. As the dense region on the lower left corner of Fig. 2c moves to the right, its height decreases. Finally, the images demonstrate that as the particles follow the streak lines their vertical drift velocity increases and horizontal (absolute) velocity decreases.

Resuspension and particles settling form the floor pattern shown in Fig. 3. The image was taken following the termination of the experiment. It covers a length of about 1/2 the wavelength (node-to-node) and consists of small ripples under the nodal regions, a thin layer under the anti-nodal region and scour in-between. A similar bed-form was reported in the past (Carter et al., 1973). The bed-form shown in Fig. 3 supports the visualization results presented in Fig. 2. Settling sediments from a near-bed small re-circulation zone form the nodal small ripples, translate in the boundary layer away from the nodes and resuspend as shown in Fig. 2. Particle sizing shows that particles at the flume floor were sorted such that their volumetric diameter was 9.8 μm under the anti-node

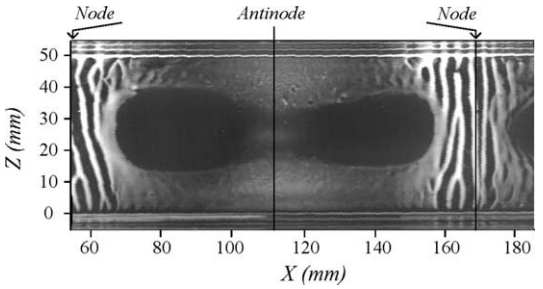

Fig. 3. A top view of the flume floor following the termination of the experiment. It shows a symmetric pattern with ripples under the nodes and light sediments under the anti-node.

(similar to the batch) and 19.96 μm at the ripples under the node. The average wavelength of the ripples shown in Fig. 3 is a few millimeters (2–5 mm) with a height of about 1.5 mm. Although a flume floor that consists of such low ripples is considered to be flat, the length-to-height ratios are similar to those reported in studies dedicated to flow over rippled beds (e.g. Sleath and Wallbridge, 2002). Our PIV measurements did not show any trace of direct vortex shedding, although extremely small vortex motion may exist. Finally, Fig. 3 shows the effect of the sidewalls, generating three-dimension flow patterns. However, the lateral orientation of the ripples and the geometrical symmetry of the bed-form support the assumption that the flow field above the floor is symmetric with a negligible mean velocity in the z direction.

3.2. PIV measurements

Our PIV results indicate that the periodic velocity field of both tracer and sediment particles is similar to the theoretical second order potential flow field (solved for the experimental conditions), with the exception that the horizontal velocity at the lower part of the flume is such that a negative velocity gradient, $\partial u/\partial y$, appears near the bed at all times. This difference seems to affect the time-averaged velocity, V_s, shown in Fig. 4, superimposed on the average vorticity map. The general feature of this velocity field is the clockwise vortex with its center around $(x, y) = (0.39\lambda, 0.4h)$. V_s is an order of magnitude smaller than the instantaneous velocity at $t = T$, and $T/2$. A close examination of V_s near the flume floor reveals a stagnation region near the resuspension location, positive x-component velocity vectors to its left and negative x-component velocity vectors to its right. A region of small velocities appears along the particle streaks region shown in Fig. 2. In addition to the large vortex, a second, much smaller, recirculation zone is detected around the nodal region. Particles that resuspend at around $x = 0.33\lambda$–0.41λ (75–93 mm), split between these two vortices. Marin and Sleath (1993) found that wave flow might generate a variety of time-average velocity fields depending on parameters such as $2\pi h/\lambda$. We have found that V_s is different from the one observed by Carter et al. (1973). Although the bed-form of both studies is basically the same, Carter et al. (1973) report on upwelling at the anti-node and settling at the node. Our results show that resuspension does not occur at the anti-node and the mass that forms the ripples arrives from the local, smaller recirculation region.

The characteristics of the periodic velocity fields were analyzed to link the velocity field with the resuspension phenomena. Shear stress, vorticity, Lagrangian velocities and turbulent

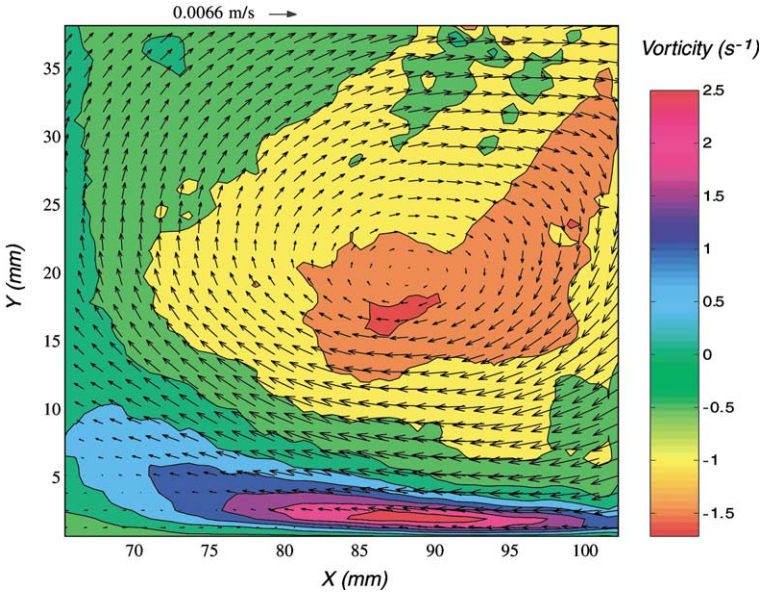

Fig. 4. Time-averaged velocity field, V_s, superimposed on the time-averaged vorticity map. A magnified plot shows a stagnation region near the bottom at $x \sim 81.5$ mm.

decomposition were calculated. Fig. 5 shows maps of $\partial\bar{u}/\partial y$ at $t = T$ and $t = T/2$. It was found that the maximum $\partial\bar{u}/\partial y$ maintains its sign and order of magnitude through all the wave phases. Fig. 5c shows a comparison between the location of maximum shear as a function of time and the temporal variation of the average resuspension location. The average resuspension location was determined by examination of a large number of resuspension events. It is shown that maximum shear is measured near the bottom and that the resuspension location oscillates in conjunction with the location of this highest shear. The observed phenomena of shear-induced resuspension deserve some attention. Particles that entrain upwards from the boundary layer would be expected to form a wide plume, since they would be fed into the mean flow field at different points along the boundary layer, and would be further dispersed by the oscillatory motion of the waves. The existence of narrow coherent particle streaks may be explained by the clear phase matching between the location of the plume and the location of the maximal $\partial\bar{u}/\partial y$.

Vorticity was calculated using the velocity field, $\overline{V}$, 16 times along the wave period. It was found that the sixteen vorticity maps are similar with no significant change in either sign or general range of values. A comparison between the vorticity and shear, $\partial\bar{u}/\partial y$ (Fig. 5), shows similarity near the bottom, indicating that $\partial\bar{u}/\partial y$ is the dominant term in the bottom vorticity.

3.2.1. Trajectories and Lagrangian velocities

Velocity fields obtained at a sufficiently high temporal resolution can be used to draw particle trajectories. We begin the calculation with the release of a particle at time t_0 and a location (x_0, y_0). Using the periodic velocity fields $(\bar{u}, \bar{v})$, the location of particles at the next time step is approximated by

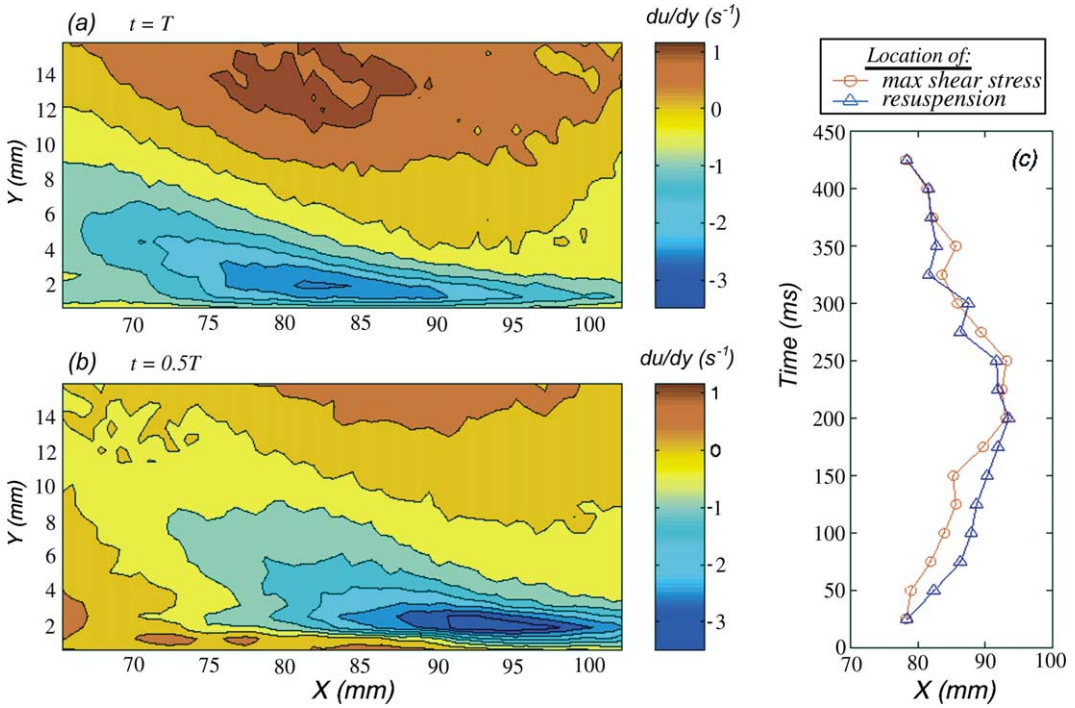

Fig. 5. Contour maps of shear rate $\partial\bar{u}/\partial y$ at $t = T$ (a) and $t = 0.5T$ (b). Location of resuspension and maximum shear $(\partial\bar{u}/\partial y)_{\max}$ versus time (c).

$$X_k = X(x_0, y_0, t_k) = X(x_0, y_0, t_{k-1}) + \bar{u}(X_{k-1}, Y_{k-1}, t_{k-1})\Delta t,$$
$$Y_k = Y(x_0, y_0, t_k) = Y(x_0, y_0, t_{k-1}) + \bar{v}(X_{k-1}, Y_{k-1}, t_{k-1})\Delta t, \tag{3}$$

where Δt is time step ($\Delta t = t_k - t_{k-1}$). Linear, parabolic and spline interpolations (in both time and space) as well as Runge–Kutta technique were tested with a wide range of time steps. It was found that linear interpolation with a small time step ($\Delta t = 1$–5 ms) provides trajectories, which are similar to the result obtained by other techniques (with differences around $\Delta y \approx 1\%$ of the single period vertical translation) but with higher computing efficiency.

The procedure was carried out to draw trajectories of particles that were released from the boundary layer and to calculate the Lagrangian mean velocity field. Fig. 6 shows the trajectories of four particles released from representative locations along the bottom. The trajectories picture overlay the time-averaged velocity field shown also in Fig. 4. The released particles move initially towards the resuspension location (the stagnation point in the time-averaged velocity field), which is expected when examining the direction of the time-averaged velocity. Particles then increase their vertical velocities, entrain into the liquid bulk and follow a well-defined wide plume that leaves the experimental section through the lower left boundary. An identical plume emerged when trajectories were calculated using the velocity field measurements of the tracer particles. A very similar symmetric plume was found for both types of particles in region #1. The actual particle streaks (shown in Fig. 2) follow approximately the path defined by the computed plume.

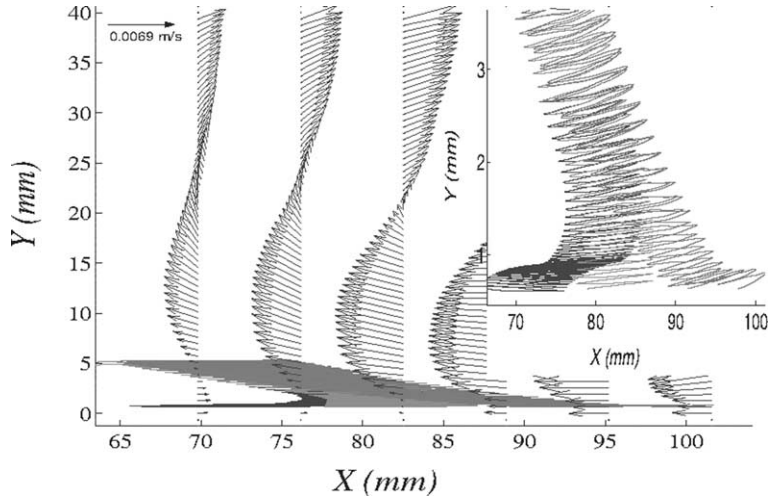

Fig. 6. Calculated trajectories of particles released at the bottom. V_s profiles at the background (same data as in Fig. 4). The inset shows a trajectories close up view.

The width of the plume is related to the earlier discussion regarding the observed thin streaks. In contrast to the visualizations in Fig. 2, which were obtained at a specific phase, the plume shown in Fig. 6 represents the overall width of oscillations. A magnification of the plume is shown in the inset providing another aspect of the transport of the resuspended particles. The significant particles vertical ascent during the wave period occurs when $\bar{u}$ is positive. A symmetric phenomenon was observed in region #1. Finally, it was found that the calculated Lagrangian velocity and measured Eulerian velocity (Fig. 4) are similar. The velocity vectors in the resuspension and sediment streak regions (lower left part of the field) are almost identical, generating the same stagnation region at the location of resuspension.

The results presented in Fig. 6 cannot provide the complete picture, as they do not include the contribution of the velocity turbulent component (u', v'). It can be expected that the turbulent field contributes to both the resuspension phenomena and to the choice of particles to 'join' either the small or large circulation regions. A major finding of our present study is that the instantaneous turbulent velocity field, (u', v'), exhibits well-defined coherent structures. The coherence of these structures is more distinguish at zero phase when the velocity changes its sign. Fig. 7 represents a sequence of consecutive turbulent maps, acquired at zero-phase, using tracer particles. It shows that the turbulent field is characterized by long-lived structures. A right-to-left slow moving vortex structure crosses the measurement area. Despite the observation that the coherence of the structures decreases when the periodic velocity is high, the structures observed at zero phase maintain their coherence during a number of periods. The ability to observe these structures in detail is very valuable for the analysis of generation of coherent structures in oscillatory flows over planar surfaces. The observed coherent structures are related to particle resuspension as was previously reported for non-periodic flows (Marchioli and Soldati, 2002). The detailed role of the vortices in inducing resuspension events is under further investigation. Our visualization shows, however, that mass balance should also be considered. Whenever the supply rate of bed-load particles is not sufficient, resuspension will be limited.

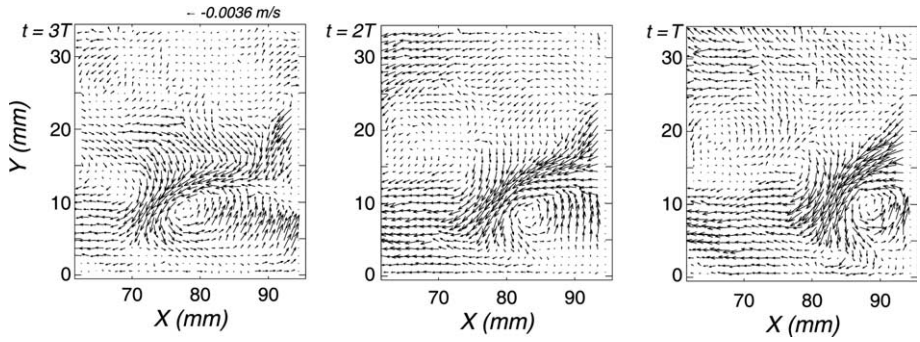

Fig. 7. Turbulent velocity maps of tracer particles measured through a sequence of three consecutive periods at zero phase. A coherent vortex is moving to the left at about 1 cm/s.

4. Conclusions

We have applied PIV to the study of resuspension and mass transport in partially standing waves. The flow velocity consists of a structured spatially and temporally periodic (partially) standing wave, and a turbulent component. It was found that the turbulent field has a much longer time scale than the periodic wave. Curiously, it maintains its coherence over these long time scales. The mean Lagrangian drift was calculated from the periodic velocity field and was found to agree with the sediment transport pattern. This pattern clearly corresponds to the vorticity field as well as to the calculated trajectories.

We have observed very narrow and well-defined streaks of sediment rising from the boundary layer. The resuspension events last a few periods, and occur intermittently. In order to study the mechanisms, which are responsible for this resuspension, we have searched for appropriate features in the velocity field, V. Two aspects need to be addressed. One is the coherent, narrow structure of the streaks. Particles entrained upwards from the boundary layer would be expected to form a wide plume. However, by analyzing the oscillatory wave field, $\overline{V}$, we found clear correlation between the location of the plume, which oscillates with the periodic field, and a marked maximum in the velocity shear $\partial\overline{u}/\partial y$, which resuspends the particles that feed the plume. Clearly, the rate of transport of the sediments depends on intra-wave processes—the correlation of the suspension concentration and the flow field.

The second aspect is the resuspension intermittency. The visualization shows that resuspension is not temporally uniform. A resuspension event may last a few periods, followed by a few tens of periods break, before the next event takes place. When studying the turbulent field, V', we found that it is characterized by long-lived structures which maintain their coherence for many wave periods. Although V' is an order of magnitude smaller than $\overline{V}$, the shear stresses due to both fields are comparable. Hence the turbulent field has a dominant role in inducing resuspension. The ability to observe these structures allows an analysis of coherent structures in oscillatory flows over planar surfaces. The vortices in the present experiment may be analogous to the well-known coherent structures from unidirectional flow wall boundary layers. The dynamics of the measured turbulent structures form a likely mechanism for the resuspension events we have observed.

References

Black, K.P., Vincent, C.E., 2001. High-resolution field measurements and numerical modeling of intra-wave sediment suspension on plane beds under shoaling waves. Coast. Eng. 42, 173–197.

Blondeaux, P., 2001. Mechanics of coastal forms. Ann. Rev. Fluid Mech. 33, 339–370.

Carter, T.G., Liu, P.L.-F., Mei, C.C., 1973. Mass transport by waves and offshore sand bedforms. J. Waterways, Harbors, Coastal Eng. 99, 165–184.

Dohmen-Janssen, C.M., 1999. Grain size influence on sediment transport in oscillatory sheet flow. In: Communications on Hydraulic and Geotechnical Engineering. Delft, The Netherlands, Report no. 99-4.

Marchioli, C., Soldati, A., 2002. Mechanisms for particle transfer and segregation in a turbulent boundary layer. J. Fluid Mech. 468, 283–315.

Marin, F., Sleath, J.F.A., 1993. Mass transport over rippled beds. In: Belorgey, M., Rajaona, R.D., Sleath, J.F.A. (Eds.), Sediments Transport Mechanisms in Coastal Environments and Rivers, Euromech 310. World Scientific.

Nielsen, P., 1992. Coastal Bottom Boundary Layers and Sediment Transport (Advanced Series on Ocean Engineering, vol. 4). World Scientific, Singapore, p. 324.

Sleath, J.F.A., Wallbridge, S., 2002. Pickup from rippled beds in oscillatory flow. J. Waterways, Port, Coastal Ocean Eng. 128, 228–237.